APPLIED SCIENCES AND ENGINEERING

Suppression of dendrite growth by cross-flow in microfluidics

Meghann C. Ma[1], Gaojin Li[2], Xinye Chen[3], Lynden A. Archer[2], Jiandi Wan[1]*

Formation of rough, dendritic deposits is a critical problem in metal electrodeposition processes and could occur in next-generation, rechargeable batteries that use metallic electrodes. Electroconvection, which originates from the coupling of the imposed electric field and a charged fluid near an electrode surface, is believed to be responsible for dendrite growth. However, few studies are performed at the scale of fidelity where root causes and effective strategies for controlling electroconvection and dendrite growth can be investigated in tandem. Using microfluidics, we showed that forced convection across the electrode surface (cross-flow) during electrodeposition reduced metal dendrite growth (97.7 to 99.4%) and delayed the onset of electroconvective instabilities. Our results highlighted the roles of forced convection in reducing dendrite growth and electroconvective instabilities and provided a route toward effective strategies for managing the consequences of instability in electrokinetics-based processes where electromigration dominates ion diffusion near electrodes.

INTRODUCTION

Application of an electric field to any liquid electrolyte confined between planar electrodes perturbs the spatial distribution of ions in the vicinity of the electrodes. At high ionic currents typical of the most practiced electrochemical processes (i.e., electrodialysis, electrodeposition, water desalination, and rechargeable batteries), the field-induced ion migration rate dominates ion transport by diffusion (*1*). At interfaces that allow selective permeation of ions of one sign, this leads to an ion concentration polarization, or the formation of a nonelectroneutral or space-charge layer (SCL) near the electrode in which the electrolyte is locally depleted of ions (*2*). Coupling of the imposed electric field and the charged fluid in the SCL imposes large body forces on the fluid, which drives a hydrodynamic instability known as electroconvection (*3*).

Electroconvection is thought to be responsible for the overlimiting current at a high DC bias and the formation of rough, dendritic deposits in metal electrodeposition processes. During the formation of the SCL, strong ion concentration polarization accompanies amplified local electrokinetic responses and electroconvective instability in the ion depletion region, resulting in a circulating, vortex-like flow pattern (*2*, *4*). Such flow pattern, according to a recent theory by Rubinstein and Zaltzman (*5*), is driven by a nonequilibrium electro-osmotic slip velocity in the extended SCL, i.e., the "second-kind" electro-osmosis compared to the first-kind electroosmosis that occurs in the quasi-equilibrium electric double layer. As a result, electroconvection enhances ion transport in an overlimiting current where ion transport would otherwise be limited by diffusion (*1*). Formation of dendrites at the electrode in metal plating, on the other hand, results from a morphological instability that fundamentally is unrelated to the hydrodynamic instability described above (*6*, *7*). However, the onset of the morphological instability breaks the cathode's flatness and induces electro/diffusion-osmotic microstreaming near the electrodes, which would feedback on the deposition (*3*). The strength of electroconvection is found to correlate tightly with the morphology of the dendrite (*3*).

To date, many efforts have been made to mitigate dendrite growth by controlling hydrodynamic instability via manipulating ion transport in the electrolyte or by reducing the local electric field near the electrode surface (*8*–*17*). Among them, incorporating additives such as carbonate-based or fluoro-based electrolytes (*8*, *9*), self-healing cations (*10*), or ionic liquids (*11*) has resulted in smooth electrodeposition. These additives served to reduce the high local electric field at nucleation sites and consequently homogenized the electric field across the surface. In addition, surface modifications, such as immobilized anions (*12*), patterned electrodes (*13*, *14*), or selective membranes (*15*, *16*), could tune the effect of ion-transport instabilities to modify electroconvection in electrodeposition. A notable study from Han *et al.* (*17*) has shown that a single deionizing shock due to surface conduction could stabilize metal electrodeposition in porous media.

Although many strategies for selectively suppressing electroconvective instabilities to avoid dendrite growth have been developed, the fundamental roles played by local fluid and ion transport dynamics near the electrode are largely overlooked and the particular roles of convective flow in dendrite formation and growth are missing (*18*, *19*). Classic studies in metal solidification have shown the effect of convective flow on dendrite growth in metal melts (*20*–*22*). These studies, however, mainly focused on fluid-solid interaction to determine permeability (*20*–*22*), and there was no externally applied electric field during dendritic solidification, which is fundamentally different with what we described here. Microfluidic-based and rotating disk approaches have observed dendrite growth in the presence of an externally applied pressure-driven flow and shear flow, respectively, during electrodeposition (*18*, *23*–*28*). These studies demonstrated the effect of flow on the morphological changes of dendrite, but flow was not correlated with the initial appearance of ramification and the relation among electroconvection, applied flow, and the kinetics of dendrite growth was missing. Here, we developed a microfluidic-based electrochemical system with simultaneous high-speed imaging and chronoamperometric/chronopotentiometric recording to investigate the effect of cross-flow on potential, current density, electroconvective vortexes, and dendrite growth kinetics during electrodeposition. A microfluidic approach (i) enables the

[1]Department of Chemical Engineering, University of California, Davis, Davis, CA 95616, USA. [2]Smith School of Chemical and Biomolecular Engineering, Cornell University, Ithaca, NY 14850, USA. [3]Department of Microsystems Engineering, Rochester Institute of Technology, Rochester, NY 14623, USA.
*Corresponding author. Email: jdwan@ucdavis.edu

real-time optical analysis of morphological changes of dendritic growth on the electrode surface, (ii) observes the formation and evolution of electroconvective vortexes, and (iii) minimizes gravitational effects on fluid motion due to its quasi–two-dimensional (2D) structure (channel height << channel width) (*3*, *29*). We hypothesize that forced convection, tangential to the electrode surface (cross-flow), supplies ions via lateral convection during electrodeposition and consequently suppresses electroconvective instability and dendrite formation. We tested our hypothesis under varied ion concentrations and potentials in the overlimiting regime and demonstrated that forced convection enhanced ion transport beyond that observed in stagnant conditions and thus attenuated electroconvective instability and suppressed dendrite formation and growth.

RESULTS

Dendrite suppression by cross-flow correlated with elevated current density and reduced current decay

Cross-flow across parallel electrodes was performed in a microfluidic channel by flowing an electrolyte solution between two strips of metal foil (Fig. 1A). Two electrode systems were considered: (i) Cu electrodes with copper sulfate pentahydrate ($CuSO_4 \cdot 5H_2O$) electrolyte and (ii) Zn electrodes with zinc sulfate heptahydrate ($ZnSO_4 \cdot 7H_2O$) electrolyte. Flow of the electrolyte and its influence on the electrode morphology and current density, *J*, were studied with chronoamperometry at a voltage of 1.5 V and an electrolyte concentration of 0.02 M. The evolution of electrode morphology and dendrite growth as functions of time were characterized with an optical microscope equipped with a high-speed camera. Figure 1B shows the representative optical images of dendrite growth during Cu electrodeposition with and without cross-flow. At each 10-s interval (30 to 60 s), the magnitude of the maximum dendrite height, H_{max}, decreased with increasing flow rate (fig. S1). At 60 s after a DC bias was applied, H_{max} was 253 ± 33.4 μm in the absence of cross-flow (Q = 0 μl/min). In the presence of cross-flow, H_{max} decreased with the increase of flow rate and was 46.9 ± 18.8 μm at Q = 200 μl/min, 81% smaller than that at Q = 0 μl/min. By averaging H_{max} over three separate locations on the electrode, we further showed that the averaged H_{max} increased linearly over time but decreased with the increase of flow rate for all tested flow rates (Fig. 1C). The dendrite growth rate, R_{avg}, which is the slope of H_{max} against time, decreased with the increase of flow rate. R_{avg} was 0.87 ± 0.015 μm/s when Q = 200 μl/min, approximately five times slower than R_{avg} at Q = 0 μl/min (4.7 ± 0.42 μm/s). Similar experiments were conducted using a zinc electrode at 1.5 V and 0.02 M; however, the zinc dendrites grew much faster and short-circuited too quickly in a stagnant solution. We performed optical recording of the zinc system at a lower potential and electrolyte concentration of 0.625 V and 0.02 M, respectively (fig. S2A). The average dendrite height, which was 173 ± 17.5 μm at Q = 0 μl/min and 6.62 ± 2.75 μm at Q = 25 μl/min, observed a 96% reduction (fig. S2B). The results showed for both metals that cross-flow with elevated flow rates suppressed dendrite formation and growth.

Chronoamperometry and optical imaging were simultaneously performed during Cu electrodeposition. The profile of current density

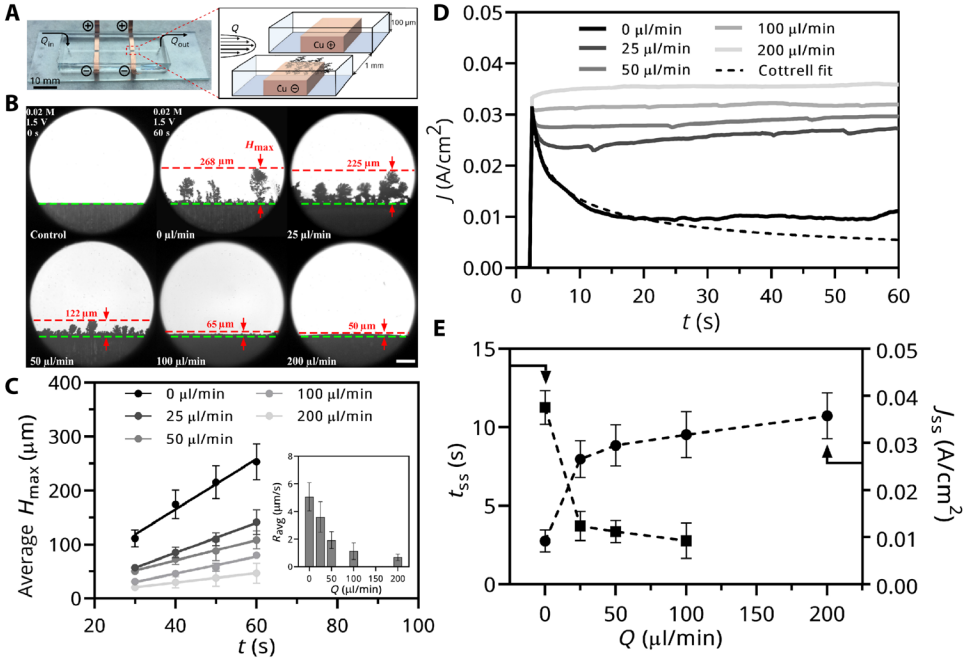

Fig. 1. Cross-flow suppressed the formation and growth of dendrites in a microfluidic-based electrochemical system. (**A**) A bright-field image of the microfluidic-based electrochemical system (left) and schematic of dendritic formation during electrodeposition of copper (right). Electrolyte: 0.02 M $CuSO_4$; voltage: 1.5 V. (**B**) Image panels showing the change of dendritic height at various flow rates (Q = 0 to 200 μl/min). The first image in the top row indicates the original position before electrodeposition and the rest of the images were taken 60 s after deposition. The green dashed line was used as the reference for measuring the dendritic height. Scale bar, 150 μm. (**C**) Average maximum dendrite height, H_{max}, increased with time but decreased in the presence of cross-flow. Inset: dendrite growth rate, R_{avg}, decreased with the increase of flow rate. (**D**) Current density *J* plotted against elapsed time of electrodeposition at varied flow rates showed increased magnitude of the steady state *J* (J_{ss}) and reduced current decay at elevated flow rates. The exponential decay at Q = 0 μl/min followed the trend predicted by the Cottrell equation (R^2 = 0.97). (**E**) The transition time (t_{ss}, left *y* axis) decreased with flow rate whereas the steady state *J* (J_{ss}, right *y* axis) increased with flow rate. Photo credit: Meghann Ma, University of California, Davis.

as a function of time changed with flow rate (Fig. 1D). Without cross-flow, the current density decayed proportionally to $t^{1/2}$ and reached a steady state, J_{ss}, when $t = 11.3 \pm 1.08$ s. The transition time, t_{ss}, was determined by the time when $\frac{\partial J}{\partial t} \approx 0$ (i.e., $\frac{\partial J}{\partial t} \leq 10^{-4}$ A/cm^2/s). Such exponential decay of current density followed the trend predicted by the Cottrell equation, $J(t) = nF D_0^{1/2} C/(\pi^{1/2} t^{1/2})$, where C is the initial cation concentration, D_0 is the diffusion coefficient of the electrolyte, n is the number of electrons, and F is Faraday's number, which suggested a diffusion-based ion transport during deposition. When cross-flow was introduced, t_{ss} decreased with the increase of flow rate and approached zero at $Q = 200$ μl/min. Meanwhile, the magnitude of J_{ss} increased with flow rate and reached 0.36 ± 0.0048 A/cm^2 at $Q = 200$ μl/min (Fig. 1E). In the Zn system, the profile of current density was similar to the copper system over increased flow rates (fig. S2C). At a higher flow rate, the system reached t_{ss} quicker, as well as maintained a larger J_{ss} of $0.027 \pm 1.3 \times 10^{-5}$ A/cm^2 at $Q = 25$ μl/min (fig. S2D). These observations showed that cross-flow regulated current density by increasing J_{ss} while reducing t_{ss} at elevated flow rates.

To further confirm the effect of cross-flow on dendrite growth, we performed additional experiments at higher electrolyte concentrations (0.1 and 0.2 M) and elevated potentials (2.0, 2.5, and 3.0 V). The results showed that the dendrite growth rate, R_{avg}, was consistently reduced in the presence of cross-flow for all trials (fig. S3). At elevated potentials, the current density did not reach steady state until a cross-flow with $Q = 200$ μl/min was applied, suggesting that suppression of stronger electroconvective instabilities at elevated potentials required high flow fields. Collectively, the suppression of dendrite growth was accomplished through forced convection, a mode of transport that could stabilize current density at higher potentials. This implied that forced convection could attenuate electroconvective instabilities and the formation of vortexes. Confirming and monitoring such instabilities, however, required operating in a constant, overlimiting current during ramification.

Cross-flow reduced the magnitude of potential at overlimiting current

We next examined dendrite growth, for both Cu and Zn electrode systems, in overlimiting currents where electroconvection was most pronounced and vortex instability drove growth. First, Cu electrodeposition was performed at a constant current density of 0.019 A/cm^2 ($J/J_{lim} = 50$) and an electrolyte concentration of 0.02 M. The limiting current J_{lim} was calculated as $J_{lim} = 4D_0FC/L$, where L is electrode distance. With increasing flow rates, both the maximum height of the Cu dendrite, H_{max}, and the growth rate of the Cu dendrite, R_{avg}, decreased, confirming that cross-flow suppressed dendrite growth in the overlimiting regime (Fig. 2, A and B). Cu dendrite growth was reduced by 99.4% at $Q = 25$ μl/min (fig. S4). Similarly, in the Zn system, electrodeposition was performed at a constant current density of 0.023 A/cm^2 ($J/J_{lim} = 50$). Optical recording showed that the magnitude of the dendrite height was suppressed by 97.7% at $Q = 50$ μl/min after 60s (fig. S5, A and B). Chronopotentiometry profiles were obtained in both electrode systems and were shaped depending on the presence of cross-flow. Figure 2C and fig. S5C showed the Cu system and Zn system, respectively, which exhibited three distinct regimes: a sharp potential overshooting regime (a) followed by a linear regime of potential decrease (a – b) and a steady-state regime (b), consistent with experimental observations conducted by Fleury *et al.* (*30*). The overshoot regime witnessed a decrease in ion concentration at the interface, which was associated with the formation of the SCL (*31*). For the Cu system, this regime occurred between $t = 0$ and a, with the highest overshooting potential at $t = 16.8 \pm 5.3$ s in the absence of flow. In the Zn system, the highest overshooting potential was also observed in the absence of flow at $t = 20.0 \pm 4.2$ s. In the presence of cross-flow, the magnitude of overshooting potential decreased with the increase of flow rates (table S1), suggesting that the maximum potential overshoot was inversely correlated with the ion concentration in the SCL and that convective flow supplemented ion transport to the SCL.

The linear regime of potential decrease occurred between a and b and extended to the end of measurement for $Q = 0$ μl/min. This linear regime of potential decrease signaled the onset of fully formed electroconvective vortexes that circulated cations and replenished the SCL. At high flow rates, the time span of the linear regime decreased and the slope of the linear regime was steeper than that of low flow rates (table S1), suggesting that forced convection alongside vortex rotation brought more cations to the electrode surface and consequently reduced potentials and suppressed electroconvective instabilities during ramification. When Q was above 10 μl/min and $Q = 25$ μl/min for the Cu and Zn system, respectively, the slope of the linear regime approached infinity, indicating that convection was the sole driving force in ion transport to the electrode surface.

Last, the steady-state regime that extended beyond region b was characterized by a constant potential (table S1) that plateaued to a lower value with increasing flow rate. The decrease in steady-state potential with increased flow rate was consistent with previously observed increased current density at elevated flow rates (Fig. 1D), induced by reduced internal resistance with a thin ion concentration polarization zone. In addition, the disappearance of the transient and linear regimes as flow rate increased coincided with the reduction of dendrite growth (Fig. 2C and fig. S5C). This implied that electroconvective instabilities, indicated by the potential overshoot and linear decrease, were suppressed in the presence of cross-flow and, as a consequence, ramification was suppressed.

When we measured the transition time, t_t, which is defined as the time when the maximum voltage overshoot transitions into a linear decrease, as an indicator of the onset of dendrite growth under flow conditions, we showed that t_t decreased with the increase of Péclet number, *Pe* (Fig. 2D). *Pe* was calculated to quantify the strength of convection using the relation $Pe = uL/D_0$ where u is the velocity. The decrease of t_t with the increase of *Pe* highlighted again that forced convection was the main driving factor responsible for delaying the onset of dendrite growth. Note that the transition time is different with Sand's time used to describe the onset dendrite growth in stagnant solutions (*32*). However, the electrochemical overshoot that signals the onset of dendrite growth is observed in our experiments.

Morphological evolution and characterization of suppressed dendrites

Scanning electron microscope (SEM) and energy-dispersive x-ray spectroscopy (EDS) were conducted for the Cu and Zn system to characterize the effects of electrolyte flow rates on the surface morphology of dendrites. We began with the Cu pristine electrode (Fig. 3A) that showed directional streaks after polishing. Using the same overlimiting current condition as Fig. 2 (current density of 0.019 A/cm^2 and electrolyte concentration of 0.02 M $CuSO_4$), we applied a low flow rate of 10 μl/min for 15 s to observe dendrite growth (Fig. 3B). Because of the fragile nature of dendrites, the exposed

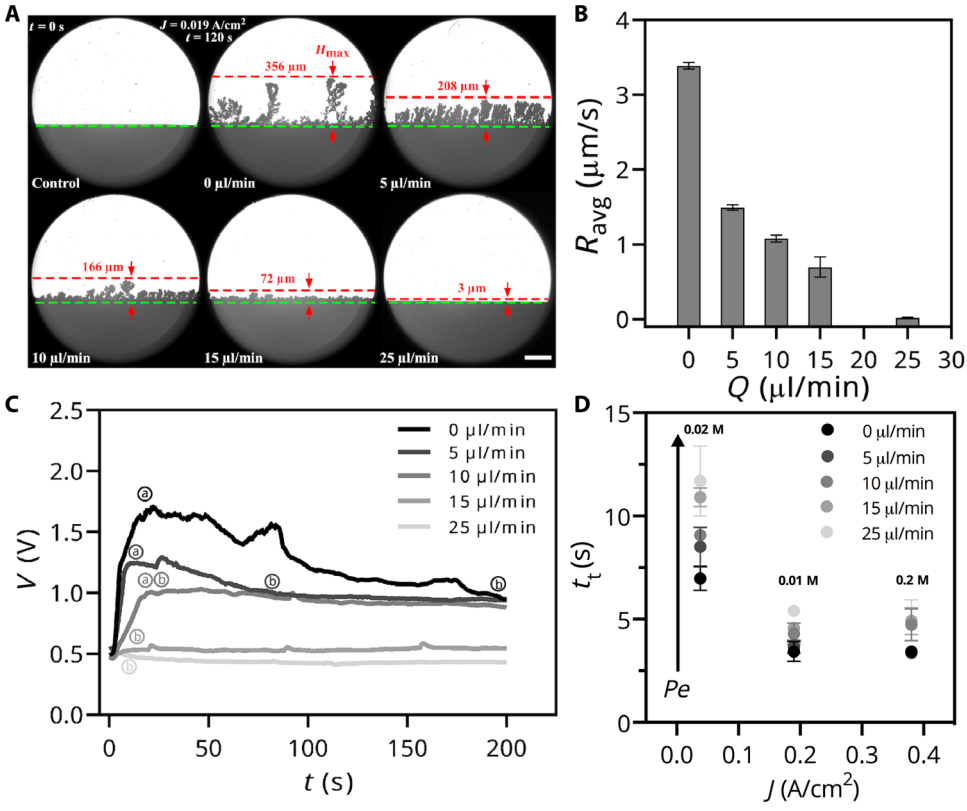

Fig. 2. Cross-flow suppressed the formation and growth of dendrites under an overlimiting current density. (**A**) Image panels showing the change of dendritic height at various flow rates (Q = 0 to 25 μl/min) under a constant overlimiting current density. The first image in the top row indicated the original position before electrodeposition and the rest of the images were taken 120 s after deposition. The green dashed line was used as the reference for measuring the dendritic height. Electrolyte: 0.02 M $CuSO_4$; current density: 0.019 A/cm^2. Scale bar, 200 μm. (**B**) Dendrite growth rate, R_{avg}, decreased with the increase in flow rate. (**C**) Potential plotted against elapsed time of electrodeposition at various flow rates (Q = 0 to 25 μl/min) showed a sharp overshooting regime (a) followed by a linear regime of potential decrease (a – b) and a steady-state regime (b). (**D**) Experimentally measured transition time, t_t, which indicated the onset of dendrite growth, decreased with current density, J, but increased with Péclet number, Pe. Experiments were performed at an electrolyte concentration of 0.02, 0.1, and 0.2 M at a current density of 0.038, 0.19, and 0.38 A/cm^2, respectively, to observe the voltage overshoot and dendrite formation at the above flow conditions.

surface of electrode after removal from the microfluidic device showed large and nonuniform debris of dendrite fractures with an average size of 1.5 ± 0.5 μm. Under full suppression of dendrite growth at Q = 25 μl/min, the electrode observed flat metal deposition (Fig. 3C), consisting of small uniform crystal bumps at 0.31 ± 0.13 μm. The average bump size was reduced by 79.3% and tightly packed; we believe that this morphology change was responsible for smooth deposition at high electrolyte flow rates compared to the tree-like dendrite structures observed in previous optical images in stagnant and lower electrolyte flow rates. A morphological assessment was also conducted using the same overlimiting condition (fig. S5) for the zinc system at a current density of 0.023 A/cm^2 and electrolyte concentration of 0.02 M. Figure 3D showed an unused, pristine zinc electrode. At a low flow rate of 25 μl/min for 15 s, the zinc electrode was covered in rose-like clusters of dendrite fractures with hexagonal crystals across the surface (Fig. 3E). The size of each rose cluster was approximately 6.5 ± 0.81 μm. Under full suppression of dendrite growth at Q = 50 μl/min, the clusters reduced in size and tightened congruently to approximately 1.3 ± 0.30 μm (Fig. 3F). Similar to the Cu system, the 80% reduction in size and tight space-filling during deposition resulted in smooth morphology at high electrolyte flow rates. EDS was conducted alongside each sample and verified that the deposited surface was Cu and Zn (fig. S6).

In addition, we measured the mass of the electrode before and after 10 min of electrodeposition for Cu (Q = 25 μl/min) and Zn (Q = 50 μl/min). The Cu experimental mass (0.064 ± 0.018 mg) was at the same order of magnitude with expected mass gain of the electrode 0.012 mg, calculated using the relationship $m = ItM_w/Fn$, where I is the current, M_w is the molecular weight, and n is the number of electrons. Similarly, the expected mass gain of the zinc electrode after 10 min of deposition at Q = 50 μl/min was 0.0075 mg, whereas the measured experimental mass was 0.0185 ± 0.0041 mg. The discrepancy of mass values between experimental and theoretical calculation was probably due to an overestimation of the volume of dendrite in experimental images where a uniform space filling (homogeneous density) of deposited metals was assumed.

Electroconvective instabilities were suppressed in cross-flow in theoretical and numerical models

To obtain fundamental insights into the effects of cross-flow on dendrite growth, we developed a theoretical model and numerical simulations to examine the convective instabilities in the overlimiting regime (SI Appendix). We conducted a linear stability analysis, a technique that has been used to study the flow effect on dendrite growth (*27*, *33*–*36*), to determine the critical voltage, V_{cr}, which is

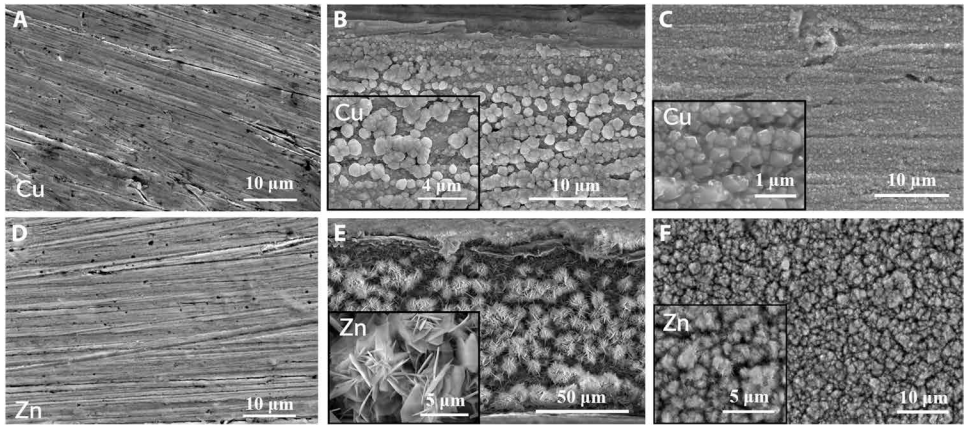

Fig. 3. Cross-flow retained the surface smoothness of electrodes. Scanning electron images of a pristine, unused electrode for (**A**) Cu and (**D**) Zn. Low flow rates of 10 and 25 μl/min for (**B**) Cu and (**E**) Zn electrodes, respectively, showing large and nonuniform clusters of dendrites. Suppressed (**C**) Cu and (**F**) Zn dendrites at high flow rates of $Q = 25$ μl/min and $Q = 50$ μl/min, respectively, showed reduced and uniform nucleation. Cu dendrite growth conditions: $A = 0.019$ A/cm^2 and 0.02 M under a flow rate of 10 μl/min for 15 s. Zn dendrite growth conditions: $A = 0.023$ A/cm^2 and 0.02 M under a flow rate of 25 μl/min for 15 s. Note that full dendrite morphology under SEM could not be observed because of the fragile nature of dendrites after microfluidic device disassembly, and the images in (B) and (E) represent debris of dendrite fractures from the electrodes.

associated with the onset of the electroconvective instability caused by the second-kind electro-osmotic slip velocity (*37*), as a function of flow velocity, U_m (Fig. 4A). The results showed that V_{cr} increased with U_m and the increment of V_{cr}, i.e., $V_{cr} - V_{cr,0}$, scaled as $V_{cr} - V_{cr,0} \sim U_m^{1/2}$, where $V_{cr,0}$ is the critical voltage at $U_m = 0$. This result showed that the imposed flow suppressed the electroconvective instability when it dominated the electro-osmotic slip velocity, u_s, which was known to scale as $u_s \sim V^2$ (*37*).

Next, we numerically calculated the current density, J, and plotted normalized current density, J/J_{lim} against U_m at varying voltages, V. Here, V was normalized by RT/F, where R is the ideal gas constant and T is the temperature. The results showed that $J/J_{lim} \sim U_m^{1/3}$ at high flow velocity (Fig. 4B), which was consistent with the classical prediction $i_n = 0.9783(nFD_0C/s_i)(u/LD_0x)^{1/3}$, where i_n is the normal component of the current density, s_i is the stoichiometric coefficient of copper, and x is the position along the electrode surface (*38*). At high voltages, the current initially decreases with increasing flow rate, showing that the enhancement of ion transport due to electroconvection was suppressed by the imposed flow. We validated the numerical results using our experimental data and showed a similar trend predicted by numerical simulations (fig. S7).

The competition between electroconvection and the imposed flow can be further observed from the concentration gradient field and the streamlines. At a small velocity (U_m = 24 μm/s), chaotic vortex pairs formed and disrupted the uniform concentration gradient creating chaotic electrolyte streamlines (Fig. 4C) (*38*). These vortexes existed in a region of ion depletion with ions circulating around the edges (*39*). In our simulation, the concentration of the cations was higher near the downwash flow region of the vortexes, revealing the connection between hydrodynamics in the electrolyte and tip growth when the arriving ions were reduced at a metal electrode. At U_m = 470 μm/s, the fluid streamlines retained a laminar feature by fully suppressing the electroconvective vortexes (Fig. 4D). In this case, the concentration gradient was uniform in comparison to that at U_m = 24 μm/s. It was worth noting that in our experiment, much higher flow velocities, e.g., 4000 to 36,000 μm/s, were required to suppress dendrite growth. The fact that the imposed flow had a stronger effect on suppressing electroconvection in the numerical

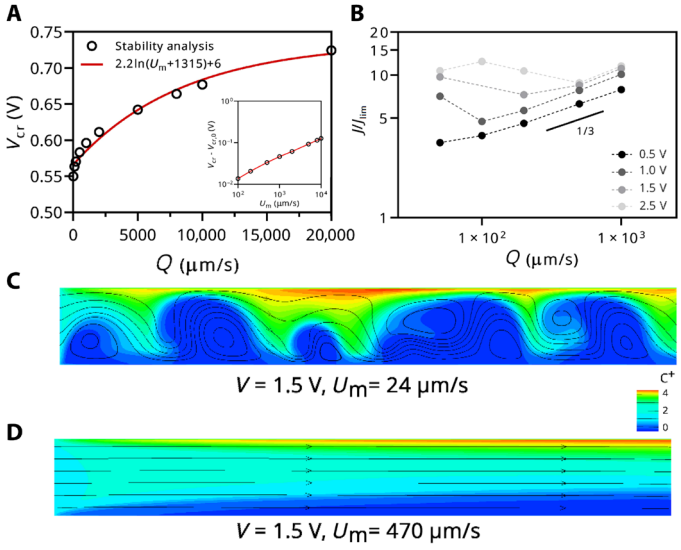

Fig. 4. Electroconvective instabilities were suppressed under cross-flow. (**A**) Linear stability analysis of the critical voltage V_{cr} against flow velocity U_m showed the delayed onset of electroconvective instabilities. Inset: the increment of V_{cr}, $V_{cr} - V_{cr,0}$, scaled as $V_{cr} - V_{cr,0} \sim U_m^{1/2}$ where $V_{cr,0}$ was the critical voltage at $U_m = 0$ μm/s. (**B**) Direct numerical simulation showed that $J/J_{lim} \sim U_m^{1/3}$ at high flow velocity. At high voltages, the current was higher at lower flow rates because of the enhanced ion transport by electroconvection, consistent with experimental results shown in fig. S7. Simulated streamline and concentration gradient at (**C**) low flow velocity (U_m = 24 μm/s) and (**D**) high flow velocity (U_m = 470 μm/s).

simulation than in the experiment was probably because the double layer thickness in simulation (~1 μm) was several orders of magnitude thicker (~1 nm) than experiment, though a thick double layer is commonly assumed in simulations because of the limitation in the grid resolution (*39*–*41*).

Cross-flow reduced electroconvective vortexes in particle-tracking experiments

To further confirm the effect of cross-flow on the delay of the onset of electroconvective instabilities, particle-tracking experiments were

performed at an electrolyte concentration of 0.02 M $CuSO_4$ and a constant current density of 9.46 mA/cm^2 (i.e., $J/J_{lim} = 25$). Note that to accurately monitor vortex evolution on the electrode surface, a relatively low current density and set of reduced flow rates were used. The electric field was applied 20 s before the application of cross-flow, $t = -20$ s, to initiate vortex formation. At $t = 0$ s, electrolyte flow was initiated through the channel to create cross-flow. Figure 5A showed representative optical images of counter-rotating vortexes with increasing flow rate at three separate time intervals. As the flow rate increased, the formation of vortexes was suppressed and there were no visible vortexes at $Q = 10$ μl/min. In particular, at low flow rates (0 to 1 μl/min), dendrite growth was observed at 32 s and the vortex flux concentrated at the tips of the dendrites (movie S1). In agreement with our simulation results, the vortexes then drove a cation flux toward the dendrite tips, resulting in ramification. Accordingly, the vortex height increased linearly with time because of the evolving strong electroconvection (Fig. 5B). At $Q = 2$ μl/min, the vortex height was constant at 130 ± 8 μm throughout the experiment and did not increase overtime, and thus, branched-out dendrite growth was not present although the electrode surface was still rough. When flow rates increased to 5 to 10 μl/min, the vortex height decreased upon the application of flow. The height of the vortex decreased 97.7% at $Q = 10$ μl/min compared to that at $Q = 0$ μl/min and fluid behavior resembled a laminar flow. As a result, there was no observable dendrite growth and the surface was smooth. Kwak *et al.* (*42*) provided scaling relations and showed that the rate of shear flow tangential to the electrode surface (cross-flow) was inversely related to the thickness of electroconvective vortexes. The relationship, $H_{vortex}/w \sim C(V^2/u_m)^{1/3}$, where w is the width of the channel, C is a calculated constant (3.24×10^{-3} A·s^2/kg·m), and u_m is the velocity, was applied to the two highest flow rates ($Q = 5$ and 10 μl/min) where potential reached a steady state at 0.38 and 0.36 V, respectively. Kwak's scaling relation predicted a vortex height of 27.2 and 20.8 μm for $Q = 5$ μl/min and $Q = 10$ μl/min, respectively. The height of the experimentally measured vortexes in this study is 27 and 13 μm, respectively. We observed a 0.7 and 37.5% difference compared to the scaling relationships.

Corroborating evidence for vortex formation was provided by chronopotentiometry measurements (Fig. 5C), which showed distinct potential profiles in response to flow rate changes. Under stagnant conditions, the potential steadily increased after the overshoot in conjunction with vortex evolution, suggesting a growing SCL. In the presence of low flow rates, i.e., $Q = 1$ and 2 μl/min, the potential increased slowly over time, whereas at high flow rates, the potential dropped sharply to a steady state. As flow rate increased from 5 to 10 μl/min, the time when the potential dropped to a steady state decreased quickly from 36.6 ± 3.55 s to 8.1 ± 3.9 s. The decrease of potential could be attributed to a consequence of cross-flow supplementing cations to the surface, thus thinning the SCL. At the highest flow rate, the potential drop occurred immediately upon application of flow because there was an instant supply of cations driven by the strong cross-flow and thus enabled uniform deposition (*43*).

We shall note that, due to the cross-flow nature, shear force may also influence the stability of electroconvection. Castellanos and Agrait (*44*) discussed for cross Poiseuille flow that transverse perturbations were greatly inhibited by forced convection whereas longitudinal perturbations were unaffected. Therefore, it was reasonable to hypothesize that cross-flow convection inhibited dendrite growth by stabilizing the tangential flux concentrated at the tips of the dendrites. Andersen *et al.* (*45*) described this phenomenon as the confinement effect: As a result of the electrolyte flow, ions could not escape in the transverse direction leading to the suppression of local electroconvective instabilities. We emphasized that although shear force might act as a confining effect, it was not strong enough to break off the dendrite structures as the observed findings showed that dendrites tilted in the direction of flow (movie S2).

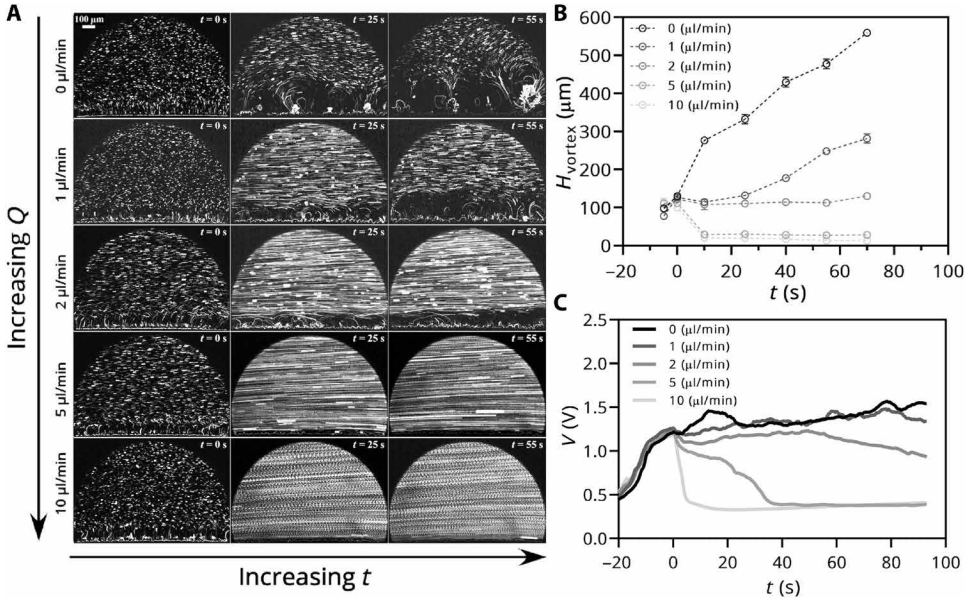

Fig. 5. Cross-flow reduced electroconvective vortexes. (**A**) Space-time plots of vortex advection at various flow rates ($Q = 0$ to 10 μl/min). Fluid flow was visualized using 1-μm polystyrene beads (6.83×10^7 particles/ml). Electrolyte: 0.02 M $CuSO_4$; current density: 9.46 mA/cm^2. Scale bar, 100 μm. (**B**) Vortex height, H_{vortex}, decreased in the presence of cross-flow. (**C**) Potential reduced in response to cross-flow during electrodeposition. $t = 0$ s in all the figures indicated the onset of applied convective flow.

DISCUSSION

The present study demonstrates that forced convection across the electrode surface during electrodeposition reduced metal dendrite growth by 97.7 to 99.4%. In addition, high flow rate resulted in an instantaneous steady-state current and steady-state potential when constant voltages and constant overlimiting currents were applied, respectively. Theoretical modeling and simulations showed that increased flow rate delayed the onset of electroconvective instabilities and created a thin concentration gradient. Additional experimental evidence using particle tracking during cross-flow further confirmed that the magnitude of electroconvective vortexes was attenuated by 97.7%. Note that at high flow rate, the current deviated from the Cottrell equation and there was a lack of both overshoot potential and a linear potential decrease commonly observed in a stagnant electrolyte, indicating that cations near the cathode were not supplied by diffusion but cross-flow. When the concentration gradient of ions stopped extending toward the bulk electrolyte owing to increased surface diffusivity (*46*) or convective flow (*42*), the thickness of the ion concentration polarization zone decreased. A thin ion concentration polarization zone implied fast ion transfer and, in our system, suggested that the cations were replenished as soon as they were reduced onto the electrode surface.

Dendrite growth was generally attributed to a morphological instability at the metal interface; however, self-enhancing dendrite growth may occur from a hydrodynamic instability known as electroconvection. The fact that reduced dendrite growth coincided with the reduction of potential induced by cross-flow indicated that ion concentration polarization, in response to a DC bias, changed with forced convection. The application of forced convection thus allowed for a regulated control of ion transport and mitigated electroconvective instabilities by reducing the ion concentration polarization and suppressing dendrite growth. Future investigations of interest should directly quantify and observe the relation between the ion concentration polarization and electroconvective instabilities to distinguish the contributions between morphological and hydrodynamic instability during dendrite growth.

MATERIALS AND METHODS

Experimental design and microfluidic fabrication

Electrochemical experiments for Cu and Zn were performed in a microfluidic device, consisting of a straight main working channel and four side channels. These channels were molded from polydimethylsiloxane over a negative pattern created by soft photolithography. The working channel had a rectangular cross section 1 mm wide and 100 μm (Zn) or 171 μm (Cu) tall, as measured by a profilometer. Two holes were created by using 1-mm Miltex biopsy punch (Integra) for injecting the electrolyte solution into the microfluidic device. These channels were sealed with a glass slide via plasma treatment. Electrolyte was introduced to the microfluidic device at various flow rates from 1 to 200 μl/min using a syringe pump (Harvard Apparatus, Pump 11 Elite). During the electrodeposition, an optical microscope (AmScope) equipped with a high-speed camera (Vision Research, Phantom VEO-710L) was used to record the dynamics of in situ electrodeposition on the surface of cathode. This camera was interfaced with Phantom PCC software, with which the continuous growth of dendrites was observed and recorded. The connection to the electrodes was made by alligator clips. The image processing was obtained by using ImageJ software. All electrochemical experiments were controlled by an electric power supply (TKD Lambda) for the chronoamperometry analysis, or a VersaSTAT 3 galvanostat (AMETEK Scientific Instruments) for the chronopotentiometry analysis. The current variation under each voltage was monitored and recorded through the 34460A digital multimeter (Keysight Technologies), which was interfaced with BenchVue software (Keysight Technologies). The dynamic potential in terms of the electrodeposition time was observed and filed by VersaStudio software (AMETEK Scientific Instruments).

Cu electrodeposition

For the Cu system, Cu foils with a thickness of 171 μm (Online Metals) were used as the cathode and anode electrodes and were embedded into the side channels. The Cu electrode had a surface area of 3.42×10^{-3} cm^2. The electrode edges were polished by 6000 grit sandpaper (Micro-Surface Finishing Products). Electrolytes containing 0.02, 0.1, and 0.2 M $CuSO_4$ were prepared using $CuSO_4 \cdot 5H_2O$ (Avantor Performance Materials), dissolved in deionized (DI) water. The electrochemical deposition for Cu was conducted for 60 s, under the applied voltage of 1.5, 2.0, 2.5, and 3.0 V, respectively. The Cu electrochemical deposition at constant current density was performed for 200 s. For the streamline tracking, the electrolyte solution was seeded with 1-μm negative carboxylate microspheres (Polysciences) and monitored under constant current density for 110 s. A nonionic surfactant (0.1 weight %), Tween 20, was added to the solution to avoid particle aggregation. The final particle concentration of the applied electrolyte solution was 6.83×10^7 particles/ml.

Zn electrodeposition

For the Zn system, Zn foils with a thickness of 100 μm (Alfa Aesar) were used as the cathode and anode electrodes. The Zn electrode had a surface area of 1.59×10^{-3} cm^2. The electrode edges were polished by 6000 grit sandpaper (Micro-Surface Finishing Products). An electrolyte containing 0.02 M $ZnSO_4$ was prepared using $ZnSO_4 \cdot 7H_2O$ (Millipore Sigma), dissolved in DI water. The electrochemical deposition for Zn was conducted for 60 s under an applied voltage of 0.625 V. The Zn electrochemical deposition at constant current density was performed for 60 s.

Measurement of mass deposited

To weigh the deposited dendrite, experiments were performed under cross-flow, $Q = 25$ μl/min and $Q = 50$ μl/min for Cu and Zn, respectively, in a constant overlimiting current ($J/J_{lim} = 50$) for 10 min. Quantification of electrodeposited mass was completed by measuring the thickness of the substrate using ImageJ after 10 min of electrodeposition and converting to the volume assuming a uniform filling (homogenous density) in 3D space. The mass was calculated using the known metal density. We note that the mass could not be calculated at lower flow rates because the dendrite growth breaks the uniform filling assumption.

SEM characterization

To image the surface of electrodes using SEM, experiments were performed under cross-flow, $Q = 25$ μl/min and $Q = 50$ μl/min for copper and zinc, respectively, in a constant overlimiting current ($J/J_{lim} = 50$) for 15 s. The electrodes were then removed from the microfluidic device manually and washed and dried at room temperature for 24 hours before SEM imaging. The SEM micrographs and EDS analysis were obtained using a Thermo Fisher Quattro S

with Kratos Supra Axis XPS. All the experiments were performed at room temperature (21°C).

SUPPLEMENTARY MATERIALS

Supplementary material for this article is available at http://advances.sciencemag.org/cgi/content/full/7/8/eabf6941/DC1

REFERENCES AND NOTES

1. E. V. Dydek, B. Zaltzman, I. Rubinstein, D. S. Deng, A. Mani, M. Z. Bazant, Overlimiting current in a microchannel. *Phys. Rev. Lett.* **107**, 118301 (2011).
2. J. N. Chazalviel, Electrochemical aspects of the generation of ramified metallic electrodeposits. *Phys. Rev. A* **42**, 7355–7367 (1990).
3. V. Fleury, J. N. Chazalviel, M. Rosso, Coupling of drift, diffusion, and electroconvection, in the vicinity of growing electrodeposits. *Phys. Rev. E* **48**, 1279–1295 (1993).
4. V. Fleury, J. Kaufman, B. Hibbert, Evolution of the space-charge layer during electrochemical deposition with convection. *Phys. Rev. E* **48**, 3831–3840 (1993).
5. I. Rubinstein, B. Zaltzman, Extended space charge in concentration polarization. *Adv. Colloid and Interface Sci.* **159**, 117–129 (2010).
6. C. P. Nielsen, H. Bruus, Morphological instability during steady electrodeposition at overlimiting currents. *Phys. Rev. E* **92**, 052310 (2015).
7. C. Chen, J. Jorne, The dynamics of morphological instability during electrodeposition. *J. Electrochem. Soc.* **138**, 3305–3311 (1991).
8. L. Oniciu, L. Mureşan, Some fundamental aspects of levelling and brightening in metal electrodeposition. *J. Appl. Electrochem.* **21**, 565–574 (1991).
9. L. Fan, H. L. Zhuang, L. Gao, Y. Lu, L. A. Archer, Regulating Li deposition at artificial solid electrolyte interphases. *J. Mater. Chem. A* **5**, 3483–3492 (2017).
10. F. Ding, W. Xu, G. L. Graff, J. Zhang, M. L. Sushko, X. Chen, Y. Shao, M. H. Engelhard, Z. Nie, J. Xiao, X. Liu, P. V. Sushko, J. Liu, J. G. Zhang, Dendrite-free lithium deposition via self-healing electrostatic shield mechanism. *J. Am. Chem. Soc.* **135**, 4450–4456 (2013).
11. A. Basile, A. I. Bhatt, A. P. O'Mullane, Stabilizing lithium metal using ionic liquids for long-lived batteries. *Nat. Commun.* **7**, ncomms11794 (2016).
12. M. D. Tikekar, L. A. Archer, D. L. Koch, Stabilizing electrodeposition in elastic solid electrolytes containing immobilized anions. *Sci. Adv.* **2**, e1600320 (2016).
13. J. Park, J. Jeong, Y. Lee, M. Oh, M. Ryou, Y. M. Lee, Micro-patterned lithium metal anodes with suppressed dendrite formation for post lithium-ion batteries. *Adv. Mater. Interfaces* **3**, 1600140 (2016).
14. S. M. Davidson, M. Wessling, A. Mani, On the dynamical regimes of pattern-accelerated electroconvection. *Sci. Rep.* **6**, 22505 (2016).
15. N. Li, W. Wei, K. Xie, J. Tan, L. Zhang, X. Luo, K. Yuan, Q. Song, H. Li, C. Shen, E. M. Ryan, L. Liu, C. Shen, Suppressing dendritic lithium formation using porous media in lithium metal-based batteries. *Nano Lett.* **18**, 2067–2073 (2018).
16. E. I. Belova, G. Y. Lopatkova, N. D. Pismenskaya, V. V. Nikonenko, C. Larchet, G. Pourcelly, Effect of anion-exchange membrane surface properties on mechanisms of overlimiting mass transfer. *J. Phys. Chem. B* **110**, 13458–13469 (2006).
17. J.-H. Han, M. Wang, P. Bai, F. R. Brushett, M. Z. Bazant, Dendrite suppression by shock electrodeposition in charged porous media. *Sci. Rep.* **6**, 28054 (2016).
18. Y. Ito, M. Nyce, R. Plivelich, M. Klein, D. Steingart, S. Banerjee, Zinc morphology in zinc–nickel flow assisted batteries and impact on performance. *J. Power Sources* **196**, 2340–2345 (2011).
19. G. González, M. Rosso, E. Chassaing, Transition between two dendritic growth mechanisms in electrodeposition. *Phys. Rev. E* **78**, 011601 (2008).
20. M. Eshraghi, M. Hashemi, B. Jelinek, S. D. Felicelli, Three-dimensional lattice Boltzmann modeling of dendritic solidification under forced and natural convection. *Metals* **7**, 474 (2017).
21. J. Madison, J. E. Spowart, D. J. Rowenhorst, L. K. Aagesen, K. Thornton, T. M. Pollock, Fluid flow and defect formation in the three-dimensional dendritic structure of nickel-based single crystals. *Metall. Mater. Trans. A* **43**, 369–380 (2012).
22. M. S. Bhat, D. R. Poirier, J. C. Heinrich, Permeability for cross flow through columnar-dendritic alloys. *Metall. Mater. Trans. B* **26**, 1049–1056 (1995).
23. M. J. Willey, U. Emekli, A. C. West, Uniformity effects when electrodepositing Cu onto resistive substrates in the presence of organic additives. *J. Electrochem. Soc.* **155**, D302 (2008).
24. A. Wlasenko, F. Soltani, D. Zakopcan, D. Sinton, G. M. Steeves, Diffusion-limited and advection-driven electrodeposition in a microfluidic channel. *Phys. Rev. E* **81**, 021601 (2010).
25. O. Crowther, A. C. West, Effect of electrolyte composition on lithium dendrite growth. *J. Electrochem. Soc.* **155**, A806 (2008).
26. J. W. Gallaway, D. Desai, A. Gaikwad, C. Corredor, S. Banerjee, D. Steingart, A lateral microfluidic cell for imaging electrodeposited zinc near the shorting condition. *J. Electrochem. Soc.* **157**, A1279 (2010).
27. J. Zheng, J. Yin, D. Zhang, G. Li, D. C. Bock, T. Tang, Q. Zhao, X. Liu, A. Warren, Y. Deng, S. Jin, A. C. Marschilok, E. S. Takeuchi, K. J. Takeuchi, C. D. Rahn, L. A. Archer, Spontaneous and field-induced crystallographic reorientation of metal electrodeposits at battery anodes. *Sci. Adv.* **6**, eabb1122 (2020).
28. J. M. Costa, M. S. Hori, A. F. de Almeida Neto, Effects of the forced convection and current density on the electrodeposition of Zn-Fe-Mo alloys. *Chem. Phys.* **527**, 110502 (2019).
29. J. M. Huth, H. L. Swinney, W. D. McCormick, A. Kuhn, F. Argoul, Role of convection in thin-layer electrodeposition. *Phys. Rev. E* **51**, 3444–3458 (1995).
30. V. Fleury, M. Rosso, J. N. Chazalviel, B. Sapoval, Experimental aspects of dense morphology in copper electrodeposition. *Phys. Rev. A* **44**, 6693–6705 (1991).
31. J. Xiao, How lithium dendrites form in liquid batteries. *Science* **366**, 426–427 (2019).
32. C. Brissot, M. Rossoa, J. N. Chazalviel, S. Lascaud, Dendritic growth mechanisms in lithium/polymer cells. *J. Power Sources* **81–82**, 925–929 (1999).
33. L. G. Sundström, F. H. Bark, On morphological instability during electrodeposition with a stagnant binary electrolyte. *Electrochim. Acta* **40**, 599–614 (1995).
34. M. D. Tikekar, L. A. Archer, D. L. Koch, Stability analysis of electrodeposition across a structured electrolyte with immobilized anions. *J. Electrochem. Soc.* **161**, A847 (2014).
35. M. N. Parekh, C. D. Rahn, L. A. Archer, Controlling dendrite growth in lithium metal batteries through forced advection. *J. Power Sources* **452**, 227760 (2020).
36. A. Huang, H. Liu, O. Manor, P. Liu, J. Friend, Enabling rapid charging lithium metal batteries via surface acoustic wave-driven electrolyte flow. *Adv. Mater.* **32**, 1907516 (2020).
37. B. Zaltzman, I. Rubinstein, Electro-osmotic slip and electroconvective instability. *J. Fluid Mech.* **579**, 173–226 (2007).
38. J. Newman, Engineering design of electrochemical systems. *Ind. Eng. Chem.* **60**, 12–27 (1968).
39. G. Li, L. A. Archer, D. L. Koch, Electroconvection in a viscoelastic electrolyte. *Phys. Rev. Lett.* **122**, 124501 (2019).
40. C. L. Druzgalski, M. B. Andersen, A. Mani, Direct numerical simulation of electroconvective instability and hydrodynamic chaos near an ion-selective surface. *Phys. Fluids* **25**, 110804 (2013).
41. E. A. Demekhin, N. V. Nikitin, V. S. Shelistov, Direct numerical simulation of electrokinetic instability and transition to chaotic motion. *Phys. Fluids* **25**, 122001 (2013).
42. R. Kwak, V. S. Pham, K. M. Lim, J. Han, Shear flow of an electrically charged fluid by ion concentration polarization: Scaling laws for electroconvective vortices. *Phys. Rev. Lett.* **110**, 114501 (2013).
43. F. Barbir, *PEM Fuel Cells: Theory and Practice* (Academic Press, 2012).
44. A. Castellanos, N. Agrait, Unipolar injection induced instabilities in plane parallel flows. *IEEE Trans. Ind. Appl.* **28**, 513–519 (1992).
45. M. B. Andersen, K. M. Wang, J. Schiffbauer, A. Mani, Confinement effects on electroconvective instability. *Electrophoresis* **38**, 702–711 (2017).
46. I. Cho, G. Y. Sung, S. J. Kim, Overlimiting current through ion concentration polarization layer: Hydrodynamic convection effects. *Nanoscale* **6**, 4620–4626 (2014).
47. A. J. Bard, L. R. Faulkner, *Electrochemical Methods Fundamentals and Applications* (John Wiley & Sons, 2001).

Acknowledgments: J.W. and M.C.M. thank the University of California, Davis for support and resources. We acknowledge the Advanced Materials Characterization and Testing Laboratory (AMCaT) for their electron imaging facility. **Funding:** L.A.A. and G.L. acknowledge support from the Department of Energy, Basic Energy Sciences Program under award no. DE-SC0016082. **Author contributions:** L.A.A. and J.W. designed research; M.C.M., G.L., and X.C. performed research; M.C.M., X.C., G.L., L.A.A., and J.W. analyzed data; and M.C.M., G.L., L.A.A., and J.W. wrote the paper. **Competing interests:** The authors declare that they have no competing interests. **Data and materials availability:** All data needed to evaluate the conclusions in the paper are present in the paper and/or the Supplementary Materials. Additional data related to this paper may be requested from the authors.

Submitted 17 November 2020
Accepted 7 January 2021
Published 19 February 2021
10.1126/sciadv.abf6941

Citation: M. C. Ma, G. Li, X. Chen, L. A. Archer, J. Wan, Suppression of dendrite growth by cross-flow in microfluidics. *Sci. Adv.* **7**, eabf6941 (2021).

Suppression of dendrite growth by cross-flow in microfluidics

Meghann C. Ma, Gaojin Li, Xinye Chen, Lynden A. Archer and Jiandi Wan

Sci Adv **7** (8), eabf6941.
DOI: 10.1126/sciadv.abf6941